Electronic Supplementary Material (ESI) for RSC Advances.

Supporting Information

Experimental details

The detailed volume ratios of solvents and mass ratios of solutes are listed in **Table S1**. Firstly, the mass ratios of solutes are fixed to be 1:1, and the volume ratios of solvents are changed to explore the optimal ratio, which comes to be 1:3. Then keep the optimal solvents ratio of 1:3 unchanged, and adjust the mass ratios of solutes to research the optimal mass ratios of solutes. Therein, the total solvents volume is 40 ml, the solutes ratio of 1:1 represents 0.125 mmol SM: 0.8 mmol TAA, and the figures of 1.5, 2, 3, 4 are the multiples of 1 SM and 1 TAA.

(1) SM:TAA=1:1					
NMP:H_2O	0:4	1:3	2:2	3:1	4:0
(2) NMP:H_2O=3:1					
SM:TAA	1:1	1:1.5	1:2	2:2	4:4

Table S1. The detailed volume ratios of solvents and mass ratios of solutes for the synthesis of MoS_2.

As shown in **Fig. S1a-e**, the MoS_2 precusor self-assembled to form MoS_2 nanosheets in which DI-water was only solvent. For the use of NMP with volume ratio of 0:4, the MoS_2 precursor formed to particle-like MoS_2 (**Fig. S1e**).

Obviously the solvents: NMP and H_2O ratio of 1:3 was the best fit in the experiment. That is because when the concentration of -OH increased with the NMP ratio, the lamellar structure could not be well formed, which directly leaded to formation of the atypical morphologies. Thus, the solvents of NMP in this experiment could limit the growth of MoS_2 crystals to be nanobowl structure rather than nanosheets.

Secondly, the weight of TAA was unilateral increased under the optimal solvents condition to explore the influence of TAA concentration. The morphologies of MoS_2 were characterized by FESEM and shown in **Fig. S1b, f-g**. It revealed that with the TAA weight increased, the aggregation getting worse and even the flower-type structure formed (**Fig. S1g**). That is because with the increase of TAA, the getting stronger van der Waal interaction drove more monolayered or bilayered nanoflakes stack to form MoS_2 sheets, then the MoS_2 sheets tended to agglomerate to minimize the surface energy, and the nanobowl structure were partly disappeared. When the ratio was increased to 1:2, the MoS_2 sheets further agglomerated to form the flower-type structure, until the system remained stable. Considering the better electrolyte penetration, we prefered the nanobowl shaped MoS_2 of the initial 1:1 ratio.

Finally, when the solvents ratio and the raw materials ratio were both under the optimal conditions, we increased the weight of SM and TAA by the same amount to twice and thrice to explore the influence of raw materials concentration. The obtained MoS_2 were denoted as MoS_2-1, MoS_2-2, and MoS_2-3. The

morphologies were characterized by FESEM and shown in **Fig. Sb, h-i**. As could be seen, the nanobowl structure basically unchanged but the dispersity weakened. To further investigate the distinction of the three products, XRD and BET analysis were employed, as shown in **Fig. S2**. The XRD (**Fig. S2a**) patterns were basically consistent, and well indexed to hexagonal MoS_2 (JCPDS Card No. 73-1508), declaring that the product were both pure MoS_2. But the BET (**Fig. S2b-d**) differed a lot, MoS_2-1, MoS_2-2, and MoS_2-3 exhibited the specific surface areas of 88.21, 65.6 and 2.2 m^2 g^{-1}, respectively. The distinction was caused by the dispersity differences, with the increase of raw materials concentration, more MoS_2 could be obtained, but the constant raw materials ratio kept the nanobowl structure basically unchanged. The increased output of MoS_2 leaded to the more frequent van der Waal interaction, so the dispersity turned weaker and less void volume could be obtained, which made the BET surface area decreased. Based on the above comparison, we conclude that NMP and H_2O ratio of 1:3 and the SM and TAA ratio of 1:1 is the optimal synthesis condition.

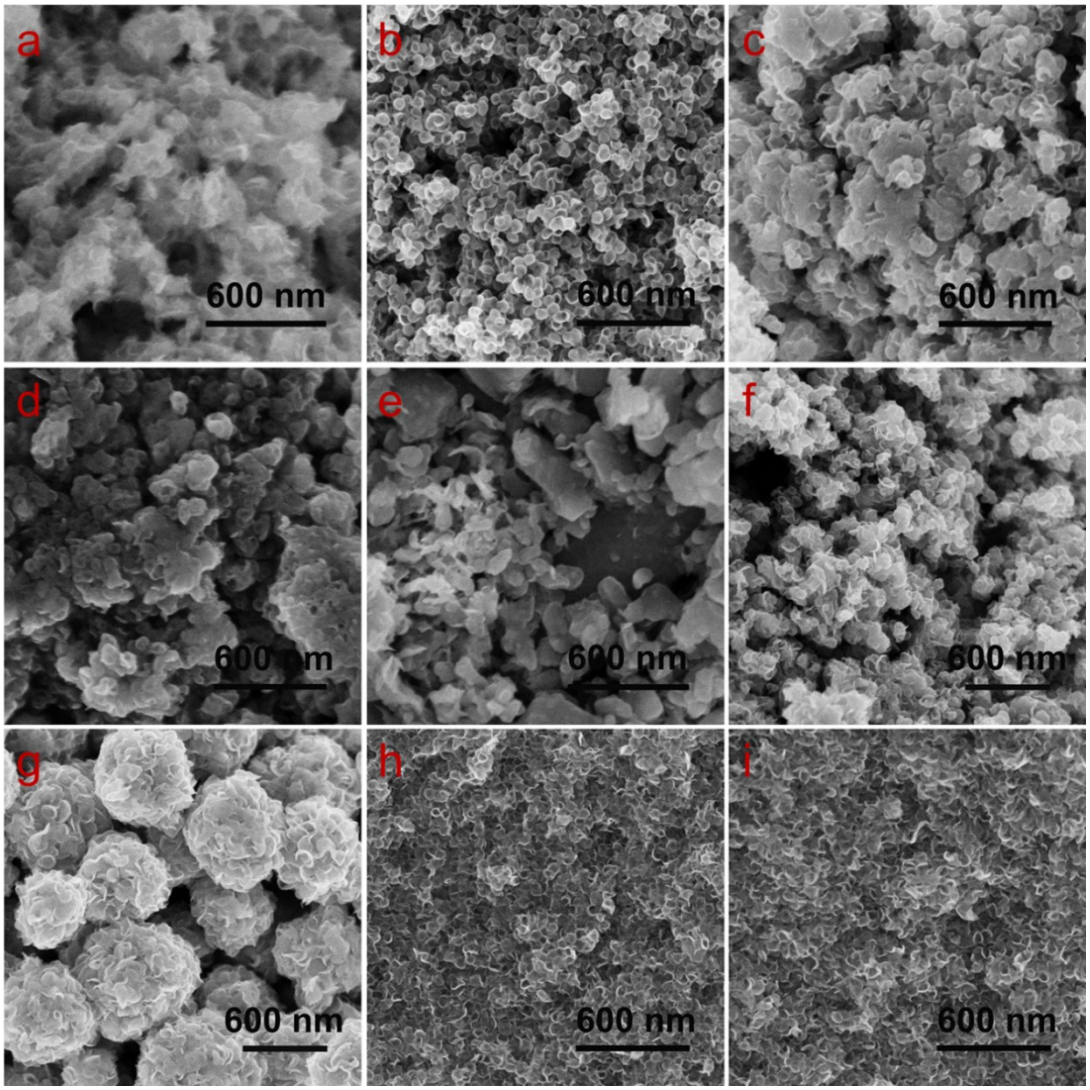

Figure S1. Morphologies of the MoS_2 nanobowls at different synthesis condition. (a-e) SEM images with the NMP and H_2O ratio of 0:4, 1:3, 2:2, 3:1and 4:0; (f-i) SEM images with the SM and TAA ratio of 1: 1.5, 1:2, 2:2 and 4:4.

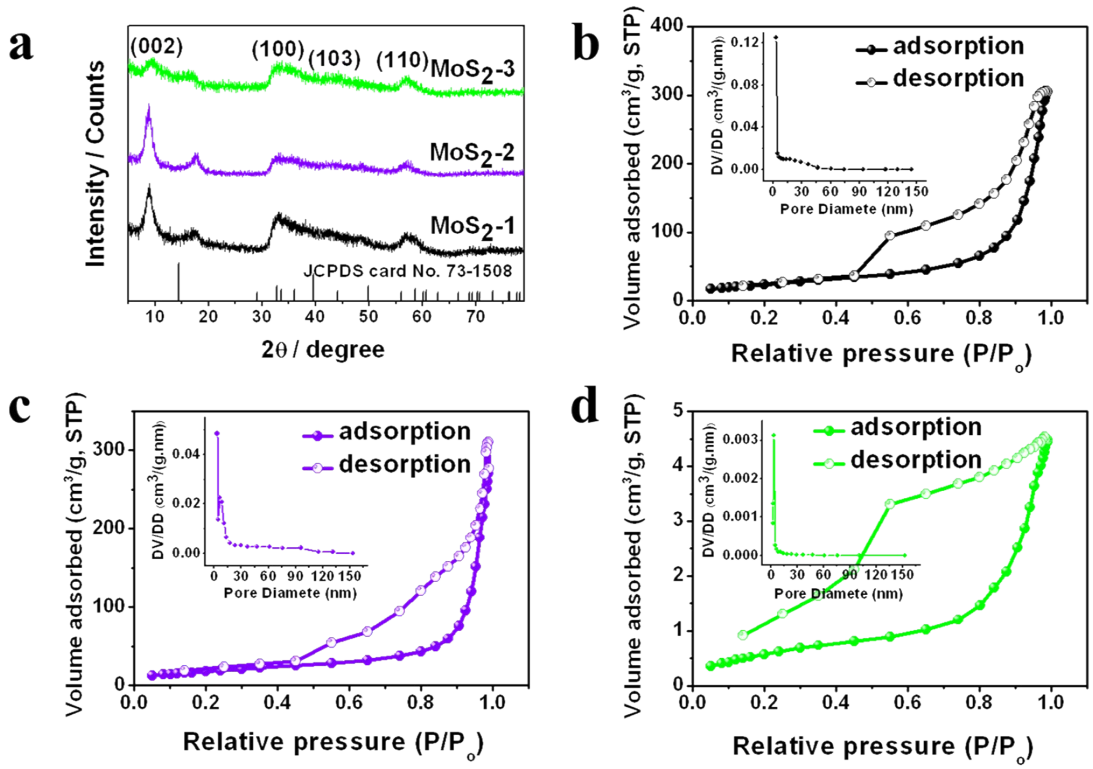

Figure S2. (a) XRD patterns and BET nitrogen adsorption and desorption isotherms of (b) MoS_2-1, (c) MoS_2-2 and (d) MoS_2-3. Inset of each plot: pore size distriution of the corresponding sample.

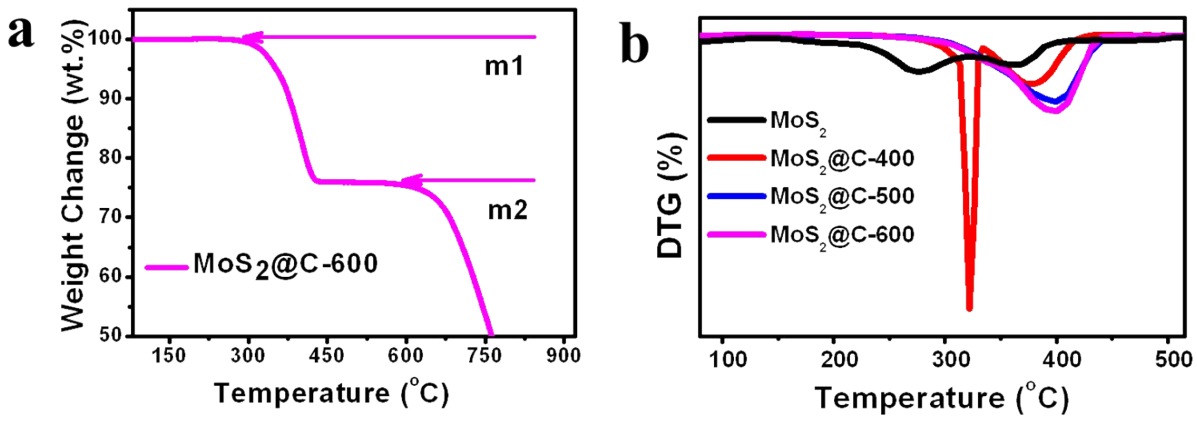

Figure S3. (a) Thermogravimetric (TG) curves MoS_2@C-600; and (b) differential thermogravimetric (DTG) curves of MoS_2, MoS_2@C-400, MoS_2@C-500, and MoS_2@C-600.

As shown in **Figure S2a**, the TGA curves of MoS_2@C-600 are mainly divided into three parts in the temperature range of 80 to 800 °C:

1. The water m(H_2O) evaporation below 200°C.

$$m_1(\text{wt.\%}) = m(MoS_2@\text{C-600}) - m(H_2O) \quad \text{(S1)}$$

2. The oxidation of MoS_2 to MoO_3 in the temperature range of 300-450°C, with gasification of carbon (m_c) in this region.

$$m_2(\text{wt.\%}) = m(MoO_3) = M(MoO_3) * n(MoO_3) \quad \text{(S2)}$$

3. The evaporation of MoO_3 in air atmosphere at temperatures higher than 680°C.

As a result, the carbon content of MoS_2@C-600 is estimated by

$$m_c(MoS_2@\text{C-600}) = m_1(\text{wt.\%}) - m_2(\text{wt.\%}) / M(MoO_3) \times M(MoS_2) = 99\ \text{wt.\%} - 75.5\ \text{wt.\%} / 144 \times 160 = 15.11\ \text{wt.\%}$$

In the same way, the carbon contents of MoS_2@C-400 and MoS_2@C-500 are also estimated to be 15.67 wt. % and 13.44 wt. %, respectively.

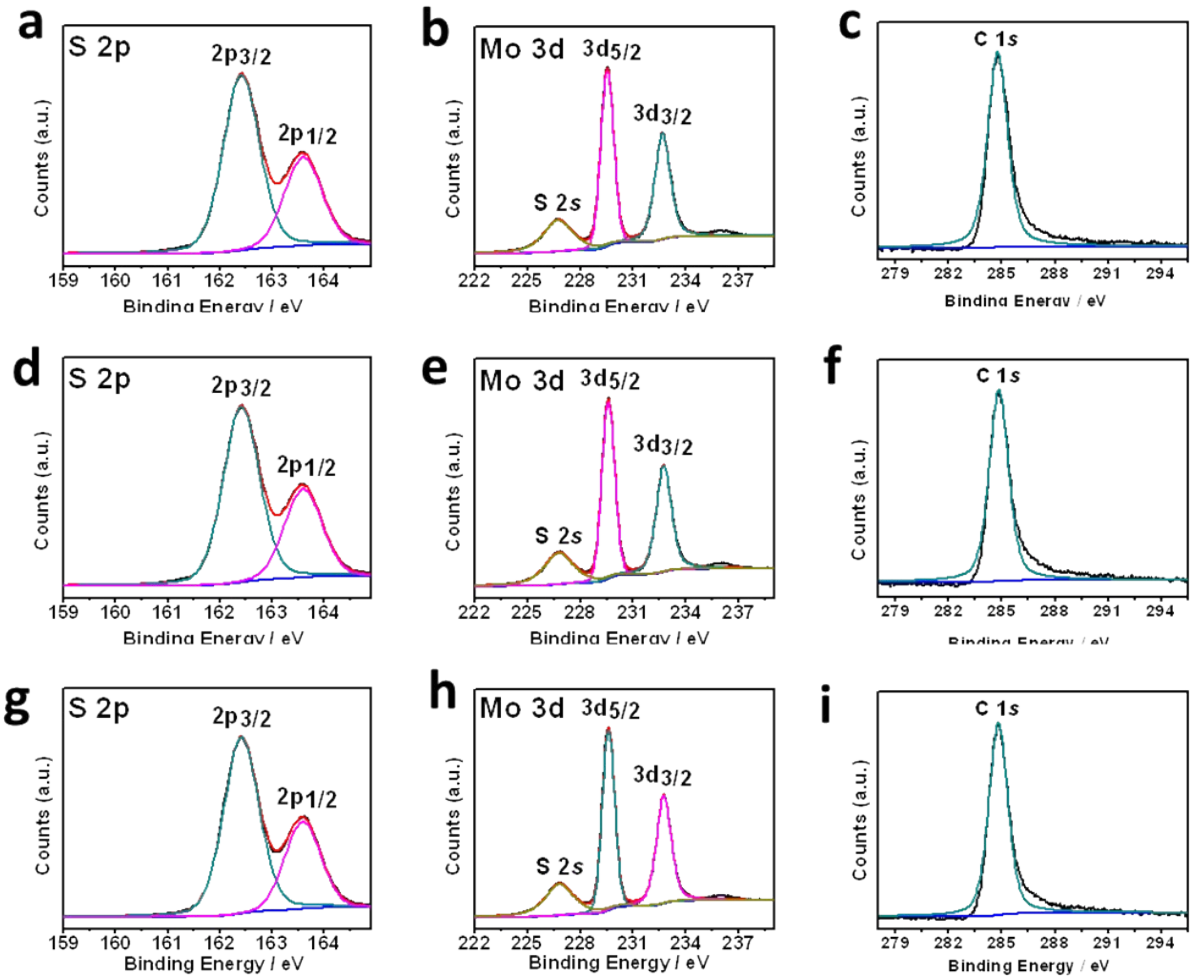

Figure S4. High resolution XPS spectra of (a) S 2p, (b) Mo 3d, and (c) C 1s for MoS_2@C-400; (d) S 2p, (e) Mo 3d, and (f) C 1s for MoS_2@C-500 and (g) S 2p, (h) Mo 3d, and (i) C 1s for MoS_2@C-600.

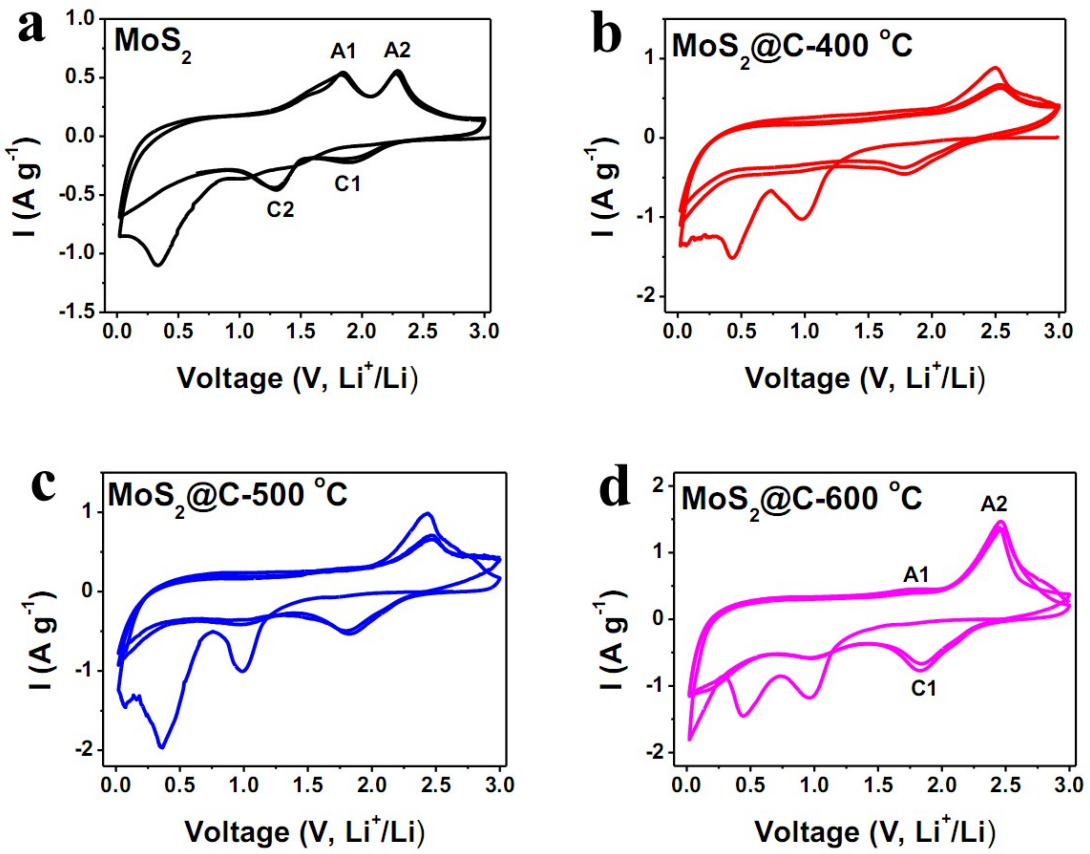

Figure S5. CV curves of the first 3 cycles for (a) MoS_2, (b) MoS_2@C-400, (c) MoS_2@C-500, and (d) MoS_2@C-600, measured at 0.2 mV s^{-1} between 0.02 and 3 V.

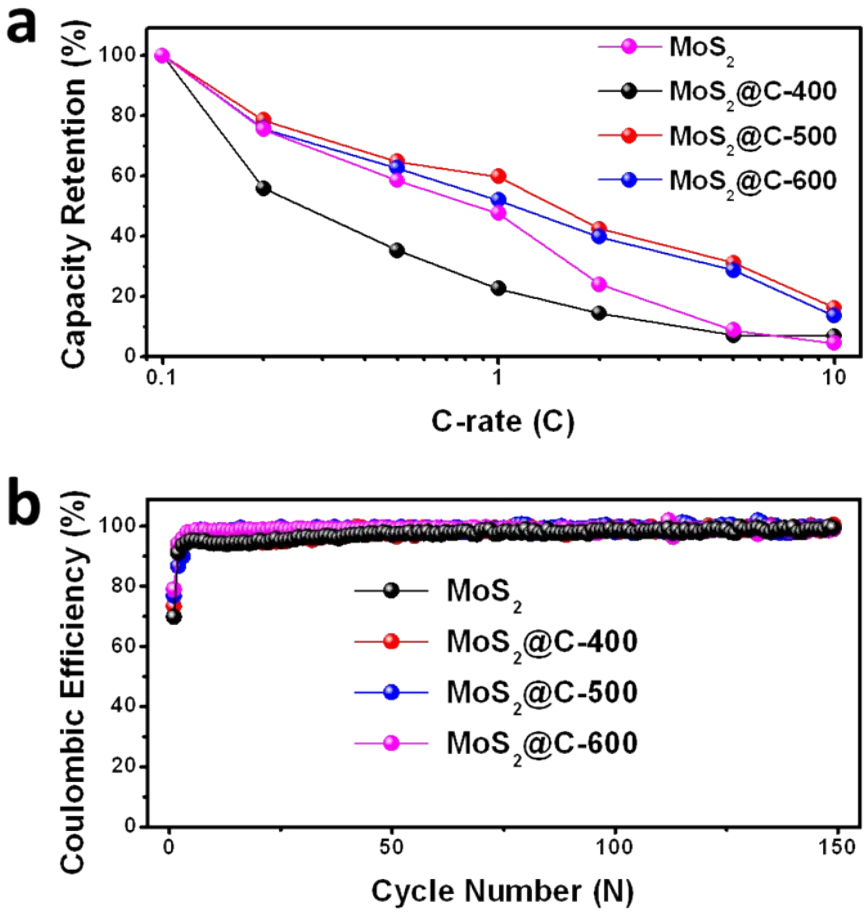

Figure S6. (a) Capacity retention vs. C-rates and (b) Coulombic efficiency of MoS_2, MoS_2@C-400, MoS_2@C-500, and MoS_2@C-600 measured at 0.2 C between 0.02 and 3 V.

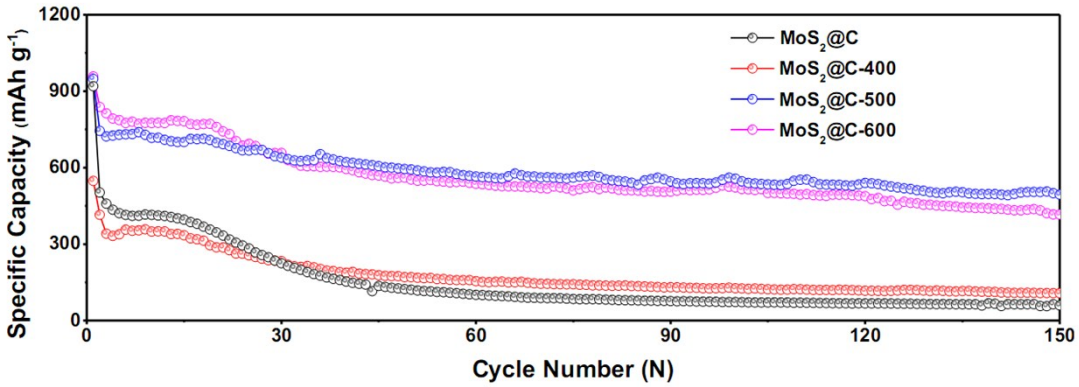

Figure S7. (a) Cycling performances of MoS_2, MoS_2@C-400, MoS_2@C-500, and MoS_2@C-600 measured at 1 C between 0.02 and 3 V.